

# Multiplication of the orbital angular momentum of phonon polaritons via sublinear dispersion

Received: 7 June 2023

Accepted: 19 February 2024

Published online: 02 April 2024

 Check for updatesAndrea Mancini<sup>1</sup>✉, Lin Nan<sup>1</sup>, Rodrigo Berté<sup>1,2</sup>, Emiliano Cortés<sup>1</sup>, Haoran Ren<sup>3</sup>✉ & Stefan A. Maier<sup>1,3,4</sup>✉

Optical vortices (OVs) promise to greatly enhance optical information capacity via orbital angular momentum multiplexing. The need for the on-chip integration of orbital angular momentum technologies has prompted research into subwavelength-confined polaritonic OVs. However, the topological order imprinted by the structure used for transduction from free-space beams to surface polaritons is inherently fixed after fabrication. Here we overcome this limitation via dispersion-driven topological charge multiplication. We switch the OV topological charge within a small frequency range (~3%) by leveraging the strong sublinear dispersion of low-loss surface phonon polaritons on silicon carbide membranes. Applying the Huygens principle, we quantitatively evaluate the topological order of experimental OVs detected by near-field imaging. We further explore the deuteronogenic effect, which predicts the coexistence of multiple topological charges in higher-order polaritonic OVs. Our work demonstrates a viable method to manipulate the topological charge of polaritonic OVs, paving the way for the exploration of novel orbital-angular-momentum-enabled light–matter interactions at mid-infrared frequencies.

Vortices with defined topological features are a ubiquitous phenomenon in physics, appearing in different systems including superconductors<sup>1</sup>, superfluids<sup>2</sup>, exciton polaritons<sup>3</sup> and magnetic materials<sup>4</sup>. Recently, propagating vortex beams characterized by twisted helical wavefronts carrying intrinsic orbital angular momentum (OAM) have been realized with electrons<sup>5</sup>, neutrons<sup>6</sup> and helium atoms<sup>7</sup>, providing a new emerging tool for the investigation of fundamental particles and interactions<sup>8</sup>. Optical vortices (OVs), the photon counterpart of such beams, constitute a theoretically unbounded set of orthogonal OAM modes, promising enhanced optical<sup>9,10</sup> and quantum<sup>11,12</sup> information processing via OAM multiplexing. Pioneered by Allen et al.<sup>13</sup>, OVs are most usually generated by spiral phase plates<sup>10</sup>, spatial light modulators<sup>9</sup> and more recently with metasurfaces<sup>14–17</sup>. Regardless of the method, the minimum size of free-space OVs is fundamentally

limited by the diffraction limit of light, whereas a reduction in the OV footprint is required for on-chip integration<sup>18–22</sup> and the unveiling of new light–matter interaction regimes<sup>23–25</sup>.

A route for realizing subwavelength OVs is by coupling optical beams into highly confined surface states such as surface plasmon polaritons (SPPs)<sup>26–32</sup> and surface phonon polaritons (SPPs)<sup>33–35</sup> through spin–orbit interactions<sup>36</sup>. However, the topological charge offered by the surface structure used for launching polaritonic OVs is always a fixed quantity after device fabrication. The imprinted topological charge  $L$  due to a propagation phase delay is proportional to the polariton momentum  $L \propto k$ , and can be then varied by the multiplication of the wavevector by an integer factor (Supplementary Note 1).

The required frequency variation to achieve a certain momentum shift is governed by the dispersion—a general property of waves

<sup>1</sup>Chair in Hybrid Nanosystems, Nanoinstitute Munich, Faculty of Physics, Ludwig-Maximilians-Universität München, München, Germany. <sup>2</sup>Instituto de Física, Universidade Federal de Goiás, Goiânia, Brazil. <sup>3</sup>School of Physics and Astronomy, Monash University, Clayton, Victoria, Australia. <sup>4</sup>Department of Physics, Imperial College London, London, UK. ✉e-mail: [A.Mancini@physik.uni-muenchen.de](mailto:A.Mancini@physik.uni-muenchen.de); [haoran.ren@monash.edu](mailto:haoran.ren@monash.edu); [s.maier@imperial.ac.uk](mailto:s.maier@imperial.ac.uk)

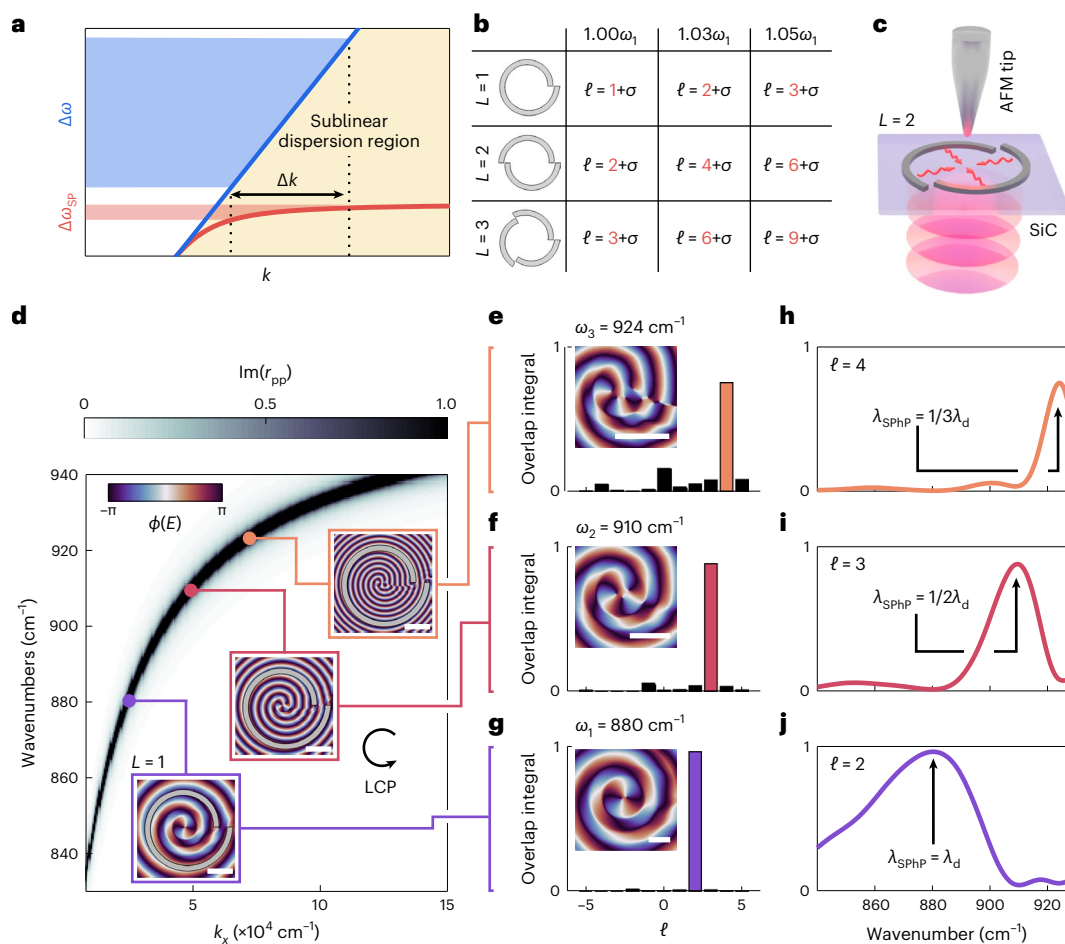


**Fig. 1 | Topological vortex multiplication via sublinear SPhP dispersion.**

**a**, Dispersion-driven tuning for free-space and polaritonic OVs based on azimuthally varying phase delay. The strong sublinear dispersion of surface polaritons results in a smaller frequency increase  $\Delta\omega_{\text{sp}}$  for the same  $\Delta k$  compared with the linear case,  $\Delta\omega$ . **b**, Changing the excitation frequency so that the momentum is increased by an integer number  $nk$  leads to OAM multiplication. The three frequencies are chosen such that the polariton momentum is  $k_1$ ,  $2k_1$  and  $3k_1$ .  $\sigma = \pm 1$  is the spin state of the incident beam. **c**, Sketch of the transmission sSNOM setup used to probe the near field of polaritonic OVs. **d**, Calculated

dispersion of the anti-symmetric mode of a 100-nm-thick SiC membrane. The insets show the simulated near-field phase maps for an SPhP vortex at three different frequencies launched by the same VG designed at  $\omega = 880 \text{ cm}^{-1}$  with  $L = 1$  and excited by LCP light. Scale bar,  $2 \mu\text{m}$ . **e–g**, Overlap integral at  $\omega = 924 \text{ cm}^{-1}$ ,  $\omega = 910 \text{ cm}^{-1}$  and  $\omega = 880 \text{ cm}^{-1}$  used to evaluate the vortex purity. The insets show the zoomed-in views of the maps shown in **d**. Scale bar,  $1 \mu\text{m}$ . **h–k**, Overlap integral for orders  $\ell = 4$ ,  $\ell = 3$  and  $\ell = 2$  as a function of excitation frequency.  $\lambda_{\text{SPhP}}$  indicates the SPhP wavelength used for VG design.

governing the propagation and light–matter interactions of electromagnetic fields. As the dispersion of light in free space is linear, doubling the momentum requires an ~100% frequency increase, making this approach impractical for most applications (Fig. 1a, blue line). In contrast, the required frequency variation for polaritonic OVs is substantially reduced due to the deeply sublinear dispersion (Fig. 1a, red curve). This small frequency change enables the flexible manipulation of the topological charge of polaritonic OVs. Even though the SPP dispersion departs from the linear behaviour, this occurs only in the region of high material losses<sup>26,37</sup>. SPhPs are characterized by low losses even in the deeply sublinear dispersion regime due to the reduced phonon–phonon scattering rate<sup>33</sup>. As such, SPhP vortices have recently been realized in a hexagonal boron nitride film on gold<sup>35</sup>; however, the measured near-field profiles of the OVs were distorted due to tilted illumination, obscuring a clear evaluation of their topological order.

Here we demonstrate dispersion-driven OAM multiplication in highly confined SPhP vortices based on suspended 100-nm-thick silicon carbide (SiC) membranes<sup>38</sup>. We realize the multiplication of polaritonic topological orders based on different surface structures with only a small (~3%) variation in excitation frequency. The topological charges

imparted from three different polariton launchers at three distinct frequencies are highlighted in red in Fig. 1b, showing the multiplication trend by a slight increase in excitation frequencies. To precisely quantify the topological order of the vortices, we introduce a set of reference functions that can be used to analyse the OAM polaritonic near-field profiles by accounting for material losses. Artefact-free amplitude- and phase-resolved near-field maps are obtained via normal-incidence transmission-type near-field microscopy (Fig. 1c). With our approach, we are able to precisely track the evolution of the experimental SPhP OAM with high mode purity through a small frequency tuning. Furthermore, we investigate the deuterogenic effect predicting the coexistence of multiple OAM modes in surface structures producing higher-order polaritonic OVs<sup>30</sup>. As a result, our demonstration presents a viable approach for the flexible manipulation of the topological charge of polaritonic OVs, paving the way for the exploration of novel OAM-enabled light–matter interactions at the subwavelength scale.

The SiC membranes we employ are fabricated with complementary-metal–oxide–semiconductor-compatible processes, resulting in large-area chips (edge length in millimetres) and precise thicknesses determined by well-established silicon-etching recipes. The remarkable

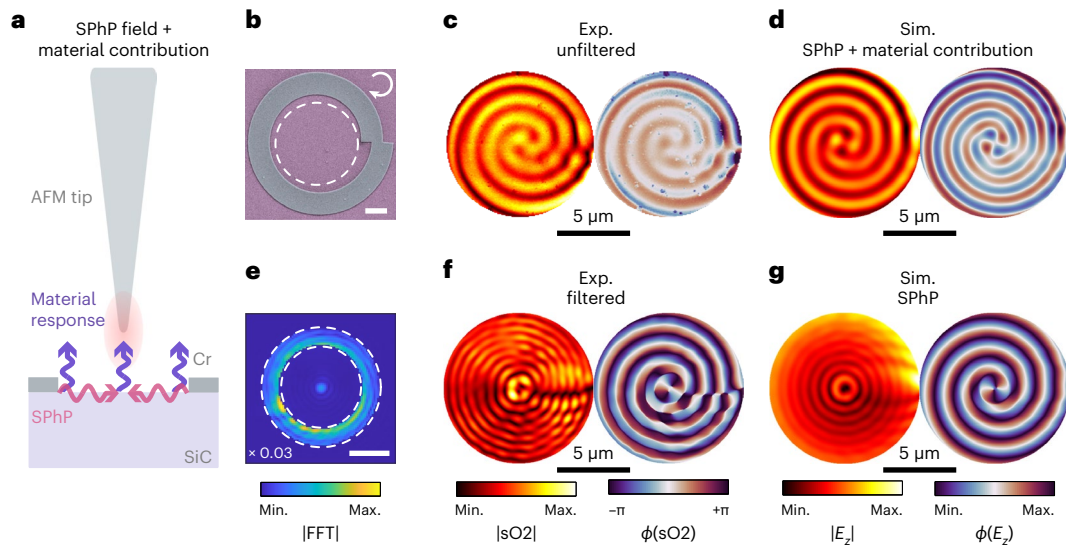


**Fig. 2 | Experimental near-field mapping of  $\ell = 2$  SPhP vortex.** **a**, In sSNOM, the pure SPhP field interferes with the bare material response. **b**, False-colour SEM image of a VG with  $L = 1$  excited by LCP light. Scale bar,  $2.5 \mu\text{m}$ . The dashed lines indicate the region where experimental data are shown. **c**, Experimental near-field amplitude  $|sO2|$  and phase  $\Phi(sO2)$  maps (second order demodulation) from the VG in **b** at  $\omega = 913 \text{ cm}^{-1}$ . **d**, Simulated corresponding vortex profile, where a

constant complex background is added to the SPhP  $E_z$  field. **e**, Removal of the material contrast through FFT filtering. Only the region between the dashed lines is retained. The rest of the map is shown multiplied by 0.03. The bright spot at the centre represents the position-independent material contrast. Scale bar,  $10k_0$ . **f**, Experimental maps obtained by the inverse FFT of the filtered data shown in **f**. **g**, Simulated corresponding SPhP  $E_z$  field.

mechanical, thermal, optical and electrical characteristics of SiC has established it as a versatile material with extensive applications, ranging from power electronics to quantum optics<sup>39–41</sup>. This versatility enhances the feasibility of implementing our approach in integrated devices.

## Results

In polar thin films, hybridization between individual SPhPs supported by the top and bottom interfaces occurs when the film thickness becomes comparable with the material skin depth<sup>38</sup>. In this regime, the splitting of the SPhP dispersion is observed, with the two modes characterized by symmetric and anti-symmetric out-of plane electric-field distributions  $E_z$  (ref. 42). In this paper, we focus on the anti-symmetric mode as it features lower losses and longer propagation lengths (Supplementary Note 2). The dispersion relation for the anti-symmetric mode of a 100 nm SiC membrane calculated through the transfer-matrix approach<sup>43</sup> is shown in Fig. 1d.

We show the dispersion-driven multiplication of an SPhP OV topological order by simulating its out-of plane electric-field component through the Huygens principle<sup>44</sup> (Supplementary Note 3). Multiple point sources are arranged in the shape of a vortex generator (VG) defined as

$$r(\varphi) = \lambda_{\text{SPhP}} \times \left( M + \frac{\text{mod}(L \times \varphi, 2\pi)}{2\pi} \right), \quad (1)$$

where  $\lambda_{\text{SPhP}}$  is the SPhP wavelength and  $\text{mod}(a, b)$  indicates the remainder of the division of  $a$  by  $b$ . Here  $L$  is the topological order of the VG determining the number of arms and  $M$  is an integer number setting its radius. A VG with  $L = 1$  and  $M = 2$  designed at  $880 \text{ cm}^{-1}$  (where the predicted SPhP wavelength is  $\lambda_d = 2.5 \mu\text{m}$ ) is used for the simulations shown in Fig. 1d. Only the phase of the calculated electric field is shown. We use the convention that anti-clockwise rotation is associated with a '+' sign, whereas clockwise rotation is indicated with a '-' sign. The SPhP phase profile under circularly polarized excitation is shown in Fig. 1d at 880, 910 and  $924 \text{ cm}^{-1}$ , where the SPhP wavelength is  $\lambda_{\text{SPhP}}^{910} = \lambda_d/2$  and  $\lambda_{\text{SPhP}}^{924} = \lambda_d/3$  corresponding to a multiplication of  $k_{\text{SPhP}}$

by a factor of 2 and 3, respectively. The total OAM  $\ell$  of the polaritonic OV at the design wavelength is given by  $\ell = L + \sigma + l$ , where  $l$  and  $\sigma = \pm 1$  are the OAM and spin states of the incident beam, respectively. In the rest of the paper, we only consider cases where the excitation beam carries no OAM; therefore,  $l = 0$ . The SPhP vortex OAM is  $\ell^{880} = 2$ ,  $\ell^{910} = 3$  and  $\ell^{924} = 4$ , as the geometrical phase delay imprinted by the VG changes from  $2\pi$  at  $880 \text{ cm}^{-1}$  to  $6\pi$  at  $924 \text{ cm}^{-1}$ .

To quantitatively assess the purity of the obtained polaritonic OVs, an overlap integral between the simulated or experimental data with a set of reference functions is commonly used<sup>17,30</sup>. Although for free-space OAM beams, Laguerre–Gaussian modes are employed as the reference, these are not suitable to represent the characteristic spiral phase pattern appearing in polaritonic OVs, which is a result of material losses. From an integral approach, we calculate the  $E_z$  value of an SPhP vortex at various  $\ell$  values, constituting a set of suitable basis functions (Supplementary Note 4). The overlap integral can be computed as a function of both topological order  $\ell$  and frequency (Supplementary Note 4). In Fig. 1e–g, the overlap spectra for the simulated maps reported in Fig. 1d are shown. The spectrum in Fig. 1g shows the high purity of the simulated  $\ell = 2$  vortex. The purity decreases in Fig. 1f, e, but the spectra clearly peak at  $\ell = 3$  and  $\ell = 4$ , as expected. The overlap integral evaluated at fixed  $\ell$  as a function of frequency is shown in Fig. 1h–j. A clear peak can be observed for  $\ell = 4$  at  $924 \text{ cm}^{-1}$ ,  $\ell = 3$  at  $910 \text{ cm}^{-1}$  and  $\ell = 2$  at  $880 \text{ cm}^{-1}$ . Intriguingly, these plots demonstrate that from theoretical simulations, a single fixed VG can lead to the creation of vortices with different topological orders. By leveraging the strong sublinear SPhP dispersion, a slight tuning of the incident frequency is sufficient to multiply the polaritonic vortex order.

To experimentally demonstrate the creation of SPhP vortices, we map the near-field pattern of the polaritonic OVs by employing transmission scattering-type scanning near-field optical microscopy (sSNOM) (Fig. 1c). Transmission sSNOM has the advantage of normal-incidence excitation and reduced tip–sample interaction, and has been the method of choice to investigate complex SPP patterns<sup>28,29,44</sup> and resonating plasmonic nanoantennas<sup>45,46</sup>. In the transmission sSNOM configuration employed for our near-field measurements, additional pathways for SPhP scattering (such as tip launched)<sup>38</sup> are

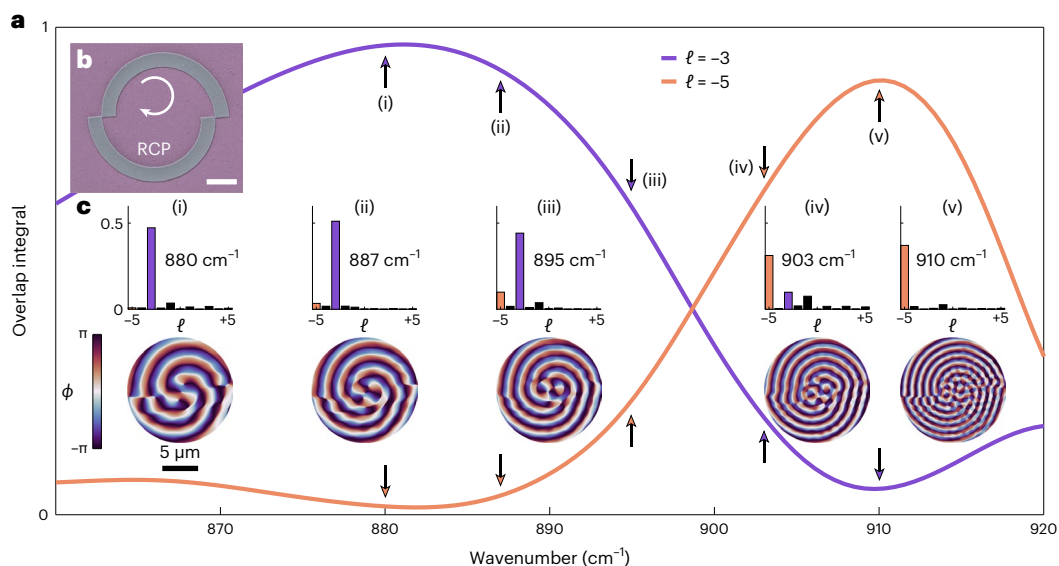


**Fig. 3 | Experimental realization of topological order multiplication via SPhP dispersion.** **a**, Simulated overlap integral as a function of frequency for an  $L = -2$  VG excited with RCP light designed at  $\omega = 880 \text{ cm}^{-1}$ . The purple and orange lines indicate overlap with  $\ell = -3$  and  $\ell = -5$  modes, respectively. **b**, False-colour SEM image of the  $L = -2$  VG used for the experiments. Scale bar,  $2.5 \mu\text{m}$ . **c**, Overlap

integral of the experimental data at different frequencies (top). The purple and orange bars correspond to  $\ell = -3$  and  $\ell = -5$ , respectively. Corresponding FFT-filtered experimental phase maps (bottom). The arrows and Roman numerals indicate the position of the predicted overlap integral at the corresponding experimental frequencies.

suppressed. Since the polarization of the incident light is perpendicular to the tip shaft, the excitation of SPhPs by the tip becomes very inefficient, leaving only the edge-launched contribution to be collected. If we instead used reflection sSNOM, where light is focused on the tip at a tilted angle, we would inevitably distort the OV pattern for multiple reasons. First, the VG design assumes excitation with a normal-incident plane wave; second, the edge-launched SPhP fringe periodicity in reflection sSNOM depends on the relative angle between the incident-beam  $k$  vector and the edge in-plane normal direction<sup>38,47</sup>, which varies along the VG geometry. In the experiments, right-circularly polarized (RCP) or left-circularly polarized (LCP) light impinges from below the sample at normal incidence. SPhPs are launched by a thin 20 nm chromium (Cr) VG fabricated by standard electron-beam lithography on a SiC membrane. The near field from the OVs is scattered by a metallic atomic force microscopy (AFM) tip, which oscillates at  $\Omega \approx 280 \text{ kHz}$  for background suppression obtained by the demodulation of the signal at  $n\Omega$ , with  $n > 1$ . The width of the VG arms is chosen to be  $2.5 \mu\text{m}$ , which we confirm is appropriate for efficient SPhP launching (Supplementary Note 6).

Due to the high transmissivity of the SiC membranes<sup>38</sup> in the mid-infrared (IR) region (100 nm thick, below the skin depth), an sSNOM signal is present even without the SPhP field excited by scattering from a Cr ridge. This uniform background field originates from the direct scattering by the sSNOM tip of the light transmitted through the membrane. As such, this contribution is usually referred to as material contrast<sup>48</sup>. As sketched in Fig. 2a, this material-dependent transmitted field interferes with the SPhP field launched by the Cr ridge, leading to the experimental sSNOM signal. The expected SPhP-only vortex amplitude and phase profiles are then qualitatively different from the experimental maps even though the material contribution is simply a uniform offset. This is because the extraction of the amplitude and phase of a complex number is not a linear operation (that is,  $|z_1 + z_2| \neq |z_1| + |z_2|$ ).

In Fig. 2b, we report a scanning electron microscopy (SEM) image of a VG with  $M = 3$  and  $L = 1$ , designed at  $\omega = 913 \text{ cm}^{-1}$  and fabricated on top of a 100 nm SiC membrane. The VG is excited with LCP light at the design frequency, and the measurements are shown for the circular region indicated by the white dashed line. Experimental amplitude

and phase maps demodulated at  $2\Omega$  are shown in Fig. 2c. The data are clipped and corrected (Supplementary Note 7). The resulting vortex is deeply subwavelength as  $\beta = \lambda_0/\lambda_{\text{SPhP}} = 7$  at this frequency. We demonstrate a maximum SPhP vortex confinement of  $\beta = 15.6$  at  $\omega = 930 \text{ cm}^{-1}$ , corresponding to  $\lambda_{\text{SPhP}} = 0.7 \mu\text{m}$  (Supplementary Note 9). The spiral pattern in the vortex amplitude can be attributed to the interference with the material background. At the same time, the phase jumps along the SPhP propagation direction are expected to go from  $-\pi$  to  $\pi$ , whereas we measure smaller oscillations. To reproduce the experimental maps, it is sufficient to add a constant complex material background  $E_{\text{mat}} = A_{\text{mat}} \exp(i\phi_{\text{mat}})$  to the simulated SPhP field. By choosing appropriate values of  $A_{\text{mat}}$  and  $\phi_{\text{mat}}$ , we obtain good agreement with the experimental maps (Fig. 2d).

The position-independent material contribution can be removed by filtering the two-dimensional fast Fourier transform (FFT) of the experimental data (Fig. 2e). As the material background is constant in space, it appears as a bright dot in the centre of the FFT map, representing a low-spatial-frequency component in Fourier space. To isolate the SPhP contribution, we multiply the FFT maps with a ring-shaped binary mask that is 1 inside the region determined by  $k_{\text{SPhP}}(\omega) \pm \Delta k$  (Fig. 2e, white dashed lines) and 0 outside. The value of  $\Delta k$  is determined as the one that better reproduces the theoretical SPhP maps. In Fig. 2e, the region to be masked is multiplied by 0.03 to show the dominant central peak associated with the material contrast. By inverse FFT, the bare SPhP contribution can be retrieved (Fig. 2f). The corresponding simulated SPhP field is shown in Fig. 2g, demonstrating good agreement with the retrieved experimental maps. We evaluate the purity of the filtered experimental data in Fig. 2f to be  $>0.6$  (Supplementary Note 4), demonstrating the high accuracy of the generated and measured SPhP OVs, allowing a clear evaluation of the topological charge.

To experimentally confirm the dispersion-driven OAM multiplication, we quantitatively assess the topological order of an SPhP vortex when changing the excitation frequency. In Fig. 3a, we report the simulated integral overlap for a VG designed at  $\omega = 880 \text{ cm}^{-1}$  with  $L = -2$  and  $M = 2$  excited by  $\sigma = -1$  RCP light. The OAM spectral analysis is performed by evaluating the overlap integral of the SPhP fields with respect to the basis functions corresponding to the total angular

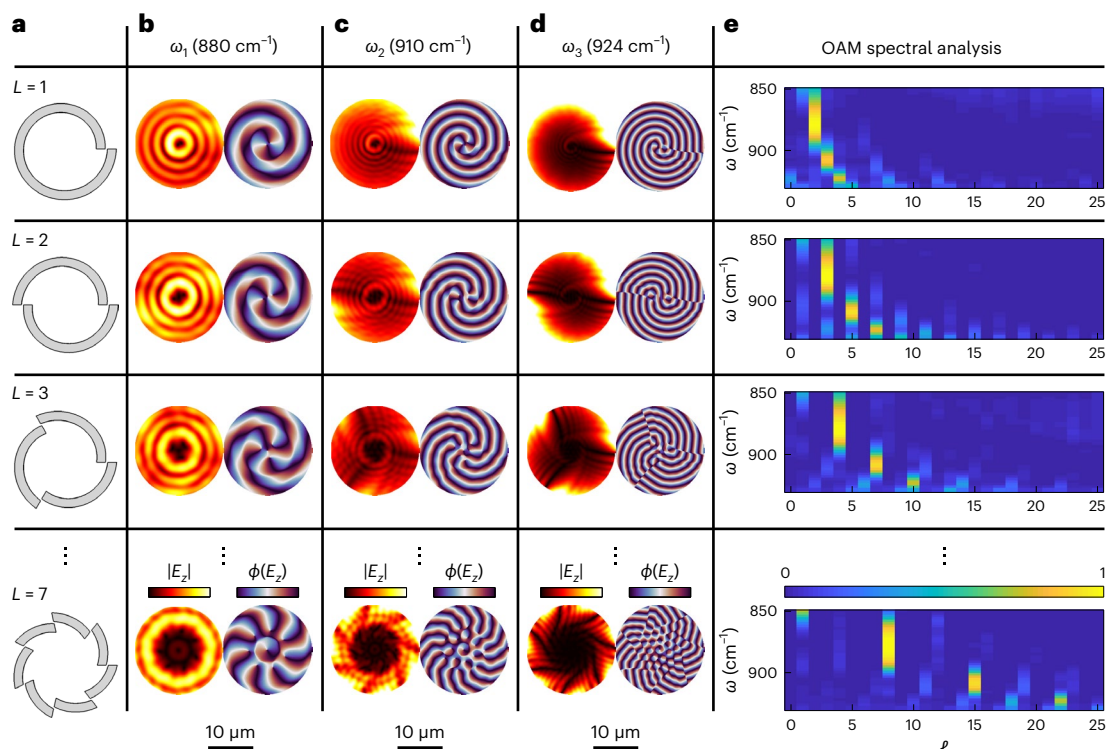


**Fig. 4 | OAM multiplication for VG with different  $L$  values under LCP excitation.** **a**, Shape of VGs with  $L = 1, 2, 3$  and **7**. **b–e**, Corresponding simulated amplitude and phase SPhP profiles at  $\omega_1 = 880 \text{ cm}^{-1}$  (**b**),  $\omega_2 = 910 \text{ cm}^{-1}$  (**c**) and  $\omega_3 = 924 \text{ cm}^{-1}$  (**d**). For each row, we calculate the overlap integral as a function

of frequency and OAM order, as shown in the maps in **e**. The maximum overlap is reached in all cases at frequencies of  $\omega_1, \omega_2$  and  $\omega_3$ . The  $\ell$  spacing between the different frequencies is  $L$ , confirming the multiplication of OAM order.

momentum of  $\ell = -3$  (Fig. 3a, purple curve) and  $\ell = -5$  (orange curve) for multiple frequencies (Supplementary Note 8).

A peak at the design frequency of  $\omega = 880 \text{ cm}^{-1}$  for  $\ell = -3$  is evident in Fig. 3a (labelled as (i)). The spectrum for  $\ell = -5$  instead shows a peak at  $\omega = 910 \text{ cm}^{-1}$  (indicated by (v)), where  $\lambda_{\text{SPhP}} = \lambda_d/2$  ( $\lambda_d$  is the SPhP wavelength at the design frequency). In Fig. 3b, we report a false-colour SEM image of the fabricated VG. We carry out experiments at five different frequencies, namely,  $\omega = 880 \text{ cm}^{-1}$ ,  $\omega = 887 \text{ cm}^{-1}$ ,  $\omega = 895 \text{ cm}^{-1}$ ,  $\omega = 903 \text{ cm}^{-1}$  and  $\omega = 910 \text{ cm}^{-1}$ , labelled from (i) to (v), respectively, in Fig. 3. For each wavelength in Fig. 3c, we report the FFT-filtered phase map along with the experimental overlap integral. We indicate the contribution at  $\ell = -3$  (purple bars) and that at  $\ell = -5$  (orange bars). The simulated values of the overlap integrals at the measured frequencies are highlighted by purple and orange arrows for  $\ell = -3$  and  $\ell = -5$ , respectively. The trend of the experimental data is in good agreement with the one from simulations, as we can track the gradual change from  $\ell = -3$  to  $\ell = -5$  as well as quantify intermediate states given by a superposition of both vortex modes. At frequencies between  $\omega = 880 \text{ cm}^{-1}$  and  $\omega = 910 \text{ cm}^{-1}$ , we expect the near-field profile to be a superposition of multiple OAM states due to mismatch between the SPhP wavelength and the VG radius. The lower absolute values of the overlap integral for the experimental results can be attributed to a number of possible discrepancies between the simulation and experimental conditions (finite width of Cr ridges, fabrication imperfections, finite laser bandwidth, slightly tilted illumination and differences between the modelled and real dielectric function of the SiC).

In Fig. 3, we experimentally demonstrated the OAM multiplication for  $L = -2$ . By simulations, we explore the same phenomena for different VGs excited by LCP light with  $L = 1, 2, 3$  and  $7$  (Fig. 4). We report the data as a table, where the rows indicate the different investigated VGs. In Fig. 4a, we show sketches of the VGs. In Fig. 4b–d, we report the

simulated amplitude and phase maps at frequencies of  $\omega_1 = 880 \text{ cm}^{-1}$ ,  $\omega_2 = 910 \text{ cm}^{-1}$  and  $\omega_3 = 924 \text{ cm}^{-1}$ , at which the SPhP momentum is doubled and tripled with respect to the one at  $\omega_1 = 880 \text{ cm}^{-1}$ . For each VG, we calculate the overlap integral as a function of both frequency and topological order (Fig. 4e). The overlap integral peaks for all the VGs are shown at three frequencies, namely,  $\omega_1, \omega_2$  and  $\omega_3$ . The OAM multiplication operation can be observed by noticing that in Fig. 4e, the adjacent maxima in  $\ell$  are spaced exactly by  $L$ . Therefore, the OAM multiplication can be applied, in principle, for any value of  $L$ .

In Fig. 4, we show that very high OAM orders can be obtained through the multiplication procedure; for  $L = 7$ , we obtain a maximum order of  $\ell = 22$  for  $\omega = 924 \text{ cm}^{-1}$ . We demonstrate that we can create and effectively measure these high-order OVs. In particular, we look into the coexistence of multiple OAM orders in polariton OVs, which has been recently shown to occur for SPPs<sup>30</sup>. This phenomena has been referred to as the ‘deuteronogenic effect’ to indicate the presence of secondary OVs as a consequence of the VG geometry used for vortex creation. According to this principle, the total OAM order of a polariton OV is given by<sup>30</sup>

$$\ell = nL + \sigma + l, \quad (2)$$

where  $n = 0, \pm 1, \pm 2, \dots$ , and  $l$  and  $\sigma = \pm 1$  are the OAM and spin states of the excitation beam, respectively. In Fig. 5a–c, we report the amplitude and phase near-field maps for vortices of order  $\ell = -10$ ,  $\ell = -15$  and  $\ell = -20$ , respectively. The measurements are performed at  $900 \text{ cm}^{-1}$  with RCP excitation. As the footprint of the higher-order vortices is larger, we use here  $M = 5$  for the definition of VGs. In Fig. 5d–f, we report the filtered amplitude and phase maps, together with the corresponding simulations shown in Fig. 5g–i. In the experimental maps, we observe a number of amplitude and phase discontinuities, which are associated with the SPhP fields launched from the combination of all the edges and sides

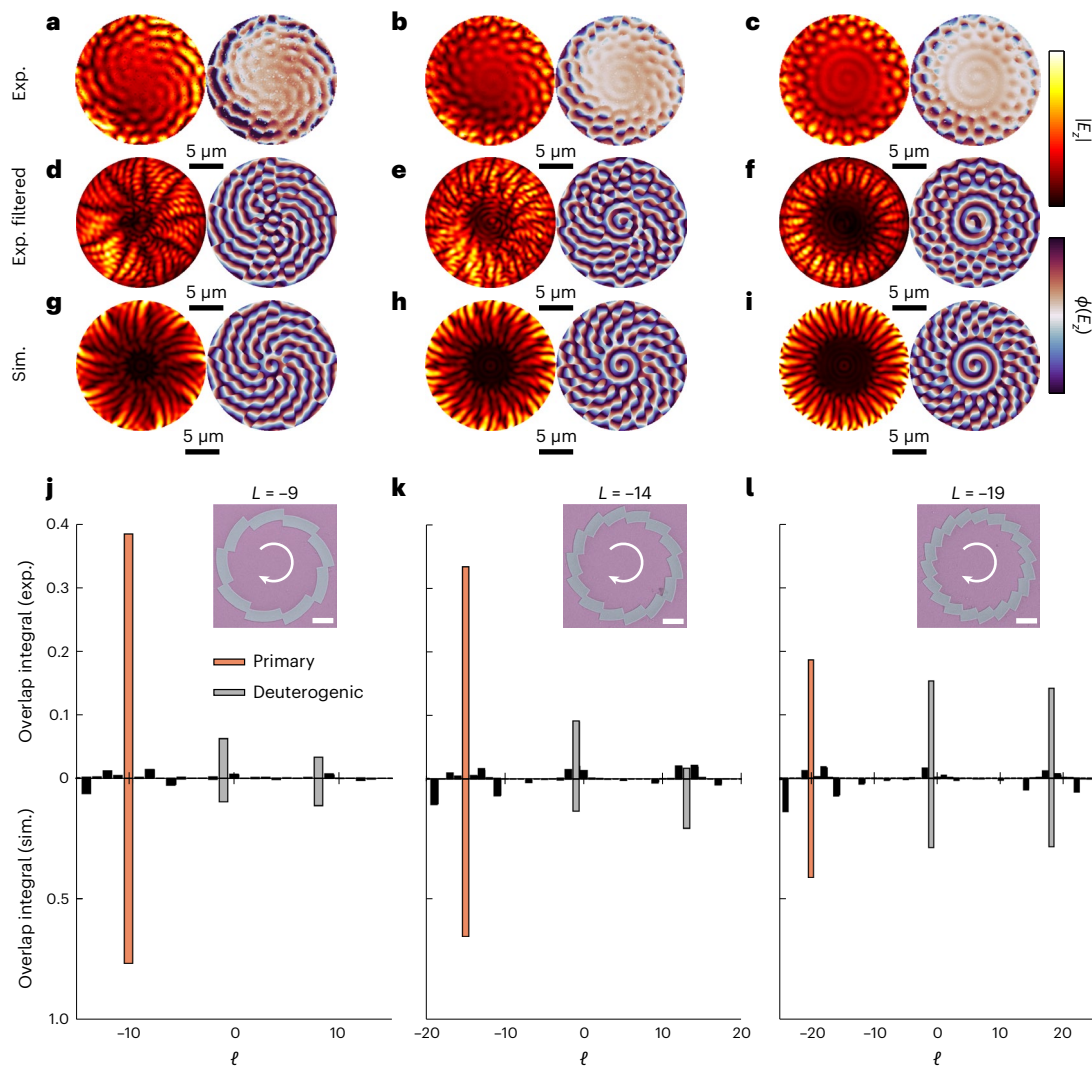


**Fig. 5 | Deuterogenic effect in high-order SPhP vortex at  $\omega = 900 \text{ cm}^{-1}$ .** **a–c**, Amplitude and phase transmission sSNOM maps at  $\omega = 900 \text{ cm}^{-1}$  for VG of  $L = -9$  (**a**),  $L = -14$  (**b**) and  $L = -19$  (**c**) excited by RCP light. **d–f**, Experimental maps after FFT filtering. **g–i**, Corresponding simulated SPhP vortex where emission from all the edges of the VG is considered. **j–l**, Overlap integrals evaluated for the

experimental data (top) and simulated data (bottom). The orange bars indicate the expected  $\ell = -10$  (**j**),  $\ell = -15$  (**k**) and  $\ell = -20$  (**l**). The grey bars indicate the values of  $\ell$  at which we detect the coexistence of additional modes predicted from the deuterogenic effect. The insets show the false-colour SEM of the fabricated VG used in the experiments. Scale bar,  $5 \mu\text{m}$ .

of the Cr ridge. To reproduce the observed discontinuities, we carried out simulations based on the Huygens principle by including the contributions from spherical sources positioned at the outer edges and sides of the fabricated Cr ridge structure (Fig. 5g–i and Supplementary Note 10). Although this effect is not pronounced for low-order SPhP vortices, it becomes apparent for higher-order SPhP vortices (Fig. 5) due to the higher number of jumps in the VG. We show the experimental (top) and simulated (bottom) overlap integrals in Fig. 5j–l together with false-colour SEM images of the Cr ridges used for SPhP launching. The overlap integrals for both simulated and experimental data present the rising of side peaks at  $\ell = -1$  and  $\ell = -L - 1$ , as consistently predicted from the deuterogenic effect. The modes associated with the deuterogenic effect are indicated by grey bars (Fig. 5j–l). We also observe that for higher  $\ell$ , the mode purity decreases due to the presence of multiple discontinuities in the VG structure. In Fig. 5j,k, we detect the coexistence of modes  $\ell = -10$  and  $\ell = -15$  with the  $\ell = -1$  order, as predicted from equation (2) for  $n = 0$  and  $\sigma = -1$ . For the  $\ell = -20$  vortex, we can also observe a strong peak at order  $\ell = 18$ , which is again expected from equation (2) for  $n = -1$ ,  $\sigma = -1$  and  $L = -19$ . Although the deuterogenic effect for  $n = 0$  and 1 has been observed for SPP<sup>30</sup>, we report here the

first experimental detection of an  $n = -1$  contribution, indicating that further terms in equation (2) have to be considered to properly describe the generated polaritonic OVs.

Intuitively, the generation of the central  $\ell = -1$  vortex can be associated with the SPhP launched by the corners of the VG arms, which overall constitute a circle of emitting dipoles. In this case, there is no additional phase delay from the structure, and the vortex  $\ell$  is equal to the sum of the spin angular momentum and OAM of the incident beam. This effect can be attenuated by reducing the number of arms of the VG and increasing the phase delay imparted by each section of the VG (Supplementary Note 12). A balance between the attenuation of the central lobe and the azimuthal distortion due to propagation losses has to be found depending on the application.

## Discussion

We leveraged the strong sublinear SPhP dispersion to obtain vortices with multiplied topological orders by a small increase of around -3% in the incident frequency. This value can be further reduced by operating at higher frequencies where the group velocity is smaller. In comparison, an approximately 100% increase in the operation frequency for

free-space beams and SPPs<sup>49</sup> is required. As SPPs are sufficiently low loss only when the dispersion is close to the light line, the smaller SPhP dissipation is a necessary ingredient to exploit the dispersion-driven OAM multiplication mechanism in a practical way. We experimentally demonstrated this tuning mechanism through the near-field mapping of mid-IR SPhP vortex in SiC-suspended membranes by transmission sSNOM. Although reconfigurable polaritonic OV can always be obtained by tuning the OAM order of the excitation beam, spatial light modulators are not readily available at mid-IR frequencies<sup>50</sup>, making our result particularly relevant for mid-IR technologies. Moreover, varying the incident-beam OAM inevitably results in a reduced SPhP-launching efficiency due to the diminished overlap between the surface structure and high-intensity part of the beam, which can be optimized only for a specific OAM value. The SiC membranes employed in this work are commercially available as millimetre-scale chips and are obtained through complementary-metal-oxide-semiconductor-compatible fabrication, making this platform readily available for different applications. We envision that our SiC membrane platform could be implemented as a source of free-space OAM beams by the far-field outcoupling of SPhPs, especially useful for long-range communication applications as the SiC operational frequency matches with the 10  $\mu\text{m}$  atmospheric transparency region. A high-speed all-optical modulation of the OAM order could then be implemented by switching the driving frequency.

We find that the measured SPhP OVs agree with simulations, finding a mode purity of  $>0.6$  for a vortex with  $\ell = 2$ . Owing to the high quality of the measured SPhP vortices, we are able to investigate high-OAM states with  $|\ell|$  up to 20. We also detect the coexistence of multiple OAM states for high-order vortices, as predicted by the deuteron effect<sup>30</sup>. The generation and precise control of highly pure SPhP vortices with high topological order paves the way for applications in structured thermal emission<sup>51</sup> and explorations of dipolar-forbidden transitions by highly confined electromagnetic fields carrying OAM<sup>23,24</sup>.

## Online content

Any methods, additional references, Nature Portfolio reporting summaries, source data, extended data, supplementary information, acknowledgements, peer review information; details of author contributions and competing interests; and statements of data and code availability are available at <https://doi.org/10.1038/s41566-024-01410-5>.

## References

- Abrikosov, A. A. The magnetic properties of superconducting alloys. *J. Phys. Chem. Solids* **2**, 199–208 (1957).
- Lounasmaa, O. V. & Thuneberg, E. Vortices in rotating superfluid <sup>3</sup>He. *Proc. Natl Acad. Sci. USA* **96**, 7760–7767 (1999).
- Lerario, G. et al. Room-temperature superfluidity in a polariton condensate. *Nat. Phys.* **13**, 837–841 (2017).
- Chmiel, F. P. et al. Observation of magnetic vortex pairs at room temperature in a planar  $\alpha\text{-Fe}_2\text{O}_3/\text{Co}$  heterostructure. *Nat. Mater.* **17**, 581–585 (2018).
- Verbeeck, J., Tian, H. & Schattschneider, P. Production and application of electron vortex beams. *Nature* **467**, 301–304 (2010).
- Sarenac, D. et al. Experimental realization of neutron helical waves. *Sci. Adv.* **8**, 2002 (2022).
- Luski, A. et al. Vortex beams of atoms and molecules. *Science* **373**, 1105–1109 (2021).
- Ivanov, I. P. Promises and challenges of high-energy vortex states collisions. *Prog. Part. Nucl. Phys.* **127**, 103987 (2022).
- Wang, J. et al. Terabit free-space data transmission employing orbital angular momentum multiplexing. *Nat. Photon.* **6**, 488–496 (2012).
- Yan, Y. et al. High-capacity millimetre-wave communications with orbital angular momentum multiplexing. *Nat. Commun.* **5**, 4876 (2014).
- Nagali, E. et al. Quantum information transfer from spin to orbital angular momentum of photons. *Phys. Rev. Lett.* **103**, 013601 (2009).
- Fickler, R. et al. Interface between path and orbital angular momentum entanglement for high-dimensional photonic quantum information. *Nat. Commun.* **5**, 4502 (2014).
- Allen, L., Beijersbergen, M. W., Spreeuw, R. & Woerdman, J. Orbital angular momentum of light and the transformation of Laguerre-Gaussian laser modes. *Phys. Rev. A* **45**, 8185 (1992).
- Pu, M. et al. Catenary optics for achromatic generation of perfect optical angular momentum. *Sci. Adv.* **1**, 1500396 (2015).
- Devlin, R. C., Ambrosio, A., Rubin, N. A., Mueller, J. B. & Capasso, F. Arbitrary spin-to-orbital angular momentum conversion of light. *Science* **358**, 896–901 (2017).
- Ren, H. & Maier, S. A. Nanophotonic materials for twisted-light manipulation. *Adv. Mater.* **35**, 2106692 (2022).
- de Oliveira, M. et al. Radially and azimuthally pure vortex beams from phase-amplitude metasurfaces. *ACS Photonics* **10**, 290–297 (2022).
- Genevet, P., Lin, J., Kats, M. A. & Capasso, F. Holographic detection of the orbital angular momentum of light with plasmonic photodiodes. *Nat. Commun.* **3**, 1278 (2012).
- Ren, H., Li, X., Zhang, Q. & Gu, M. On-chip noninterference angular momentum multiplexing of broadband light. *Science* **352**, 805–809 (2016).
- Yue, Z., Ren, H., Wei, S., Lin, J. & Gu, M. Angular-momentum nanometrology in an ultrathin plasmonic topological insulator film. *Nat. Commun.* **9**, 4413 (2018).
- Ji, Z. et al. Photocurrent detection of the orbital angular momentum of light. *Science* **368**, 763–767 (2020).
- Ren, H. et al. Orbital-angular-momentum-controlled hybrid nanowire circuit. *Nano Lett.* **21**, 6220–6227 (2021).
- Machado, F., Rivera, N., Buljan, H., Soljačić, M. & Kaminer, I. Shaping polaritons to reshape selection rules. *ACS Photonics* **5**, 3064–3072 (2018).
- Konzelmann, A. M., Krüger, S. O. & Giessen, H. Interaction of orbital angular momentum light with Rydberg excitons: modifying dipole selection rules. *Phys. Rev. B* **100**, 115308 (2019).
- Ni, J. et al. Gigantic vortical differential scattering as a monochromatic probe for multiscale chiral structures. *Proc. Natl Acad. Sci. USA* **118**, 2020055118 (2021).
- Maier, S. A. *Plasmonics: Fundamentals and Applications* Vol. 1 (Springer, 2007).
- Kim, H. et al. Synthesis and dynamic switching of surface plasmon vortices with plasmonic vortex lens. *Nano Lett.* **10**, 529–536 (2010).
- David, A., Gjonaj, B., Blau, Y., Dolev, S. & Bartal, G. Nanoscale shaping and focusing of visible light in planar metal-oxide-silicon waveguides. *Optica* **2**, 1045–1048 (2015).
- David, A., Gjonaj, B. & Bartal, G. Two-dimensional optical nanovortices at visible light. *Phys. Rev. B* **93**, 121302 (2016).
- Yang, Y. et al. Deuteron plasmonic vortices. *Nano Lett.* **20**, 6774–6779 (2020).
- Bai, Y., Yan, J., Lv, H. & Yang, Y. Plasmonic vortices: a review. *J. Opt.* **24**, 084004 (2022).
- Prinz, E., Hartelt, M., Spektor, G., Orenstein, M. & Aeschlimann, M. Orbital angular momentum in nanoplasmonic vortices. *ACS Photonics* **10**, 340–367 (2023).
- Caldwell, J. D. et al. Low-loss, infrared and terahertz nanophotonics using surface phonon polaritons. *Nanophotonics* **4**, 44–68 (2015).
- Xiong, L. et al. Polaritonic vortices with a half-integer charge. *Nano Lett.* **21**, 9256–9261 (2021).

35. Wang, M. et al. Spin-orbit-locked hyperbolic polariton vortices carrying reconfigurable topological charges. *eLight* **2**, 12 (2022).
36. Bliokh, K. Y., Rodríguez-Fortuño, F. J., Nori, F. & Zayats, A. V. Spin-orbit interactions of light. *Nat. Photon.* **9**, 796–808 (2015).
37. Khurgin, J. B. How to deal with the loss in plasmonics and metamaterials. *Nat. Nanotechnol.* **10**, 2–6 (2015).
38. Mancini, A. et al. Near-field retrieval of the surface phonon polariton dispersion in free-standing silicon carbide thin films. *ACS Photonics* **9**, 3696–3704 (2022).
39. Zhang, X. et al. Challenges and strategies in high-accuracy manufacturing of the world's largest SiC aspheric mirror. *Light Sci. Appl.* **11**, 310 (2022).
40. Castelletto, S. et al. Silicon carbide photonics bridging quantum technology. *ACS Photonics* **9**, 1434–1457 (2022).
41. Eddy Jr, C. & Gaskill, D. Silicon carbide as a platform for power electronics. *Science* **324**, 1398–1400 (2009).
42. Dionne, J., Sweatlock, L., Atwater, H. & Polman, A. Planar metal plasmon waveguides: frequency-dependent dispersion, propagation, localization, and loss beyond the free electron model. *Phys. Rev. B* **72**, 075405 (2005).
43. Passler, N. C. & Paarmann, A. Generalized 4×4 matrix formalism for light propagation in anisotropic stratified media: study of surface phonon polaritons in polar dielectric heterostructures. *J. Opt. Soc. Am. B* **34**, 2128–2139 (2017).
44. Tsesses, S., Cohen, K., Ostrovsky, E., Gjonaj, B. & Bartal, G. Spin-orbit interaction of light in plasmonic lattices. *Nano Lett.* **19**, 4010–4016 (2019).
45. Schnell, M., Garcia-Etxarri, A., Alkorta, J., Aizpurua, J. & Hillenbrand, R. Phase-resolved mapping of the near-field vector and polarization state in nanoscale antenna gaps. *Nano Lett.* **10**, 3524–3528 (2010).
46. Bohn, B. J. et al. Near-field imaging of phased array metasurfaces. *Nano Lett.* **15**, 3851–3858 (2015).
47. Kaltenecker, K. J. et al. Mono-crystalline gold platelets: a high-quality platform for surface plasmon polaritons. *Nanophotonics* **9**, 509–522 (2020).
48. Tamagnone, M. et al. Ultra-confined mid-infrared resonant phonon polaritons in van der Waals nanostructures. *Sci. Adv.* **4**, 7189 (2018).
49. Bai, Y., Zhang, Q. & Yang, Y. Generation of tunable plasmonic vortices by varying wavelength of incident light. *Photonics* **9**, 809 (2022).
50. Fan, K., Suen, J. Y. & Padilla, W. J. Graphene metamaterial spatial light modulator for infrared single pixel imaging. *Opt. Express* **25**, 25318–25325 (2017).
51. Overvig, A. C., Mann, S. A. & Alù, A. Thermal metasurfaces: complete emission control by combining local and nonlocal light-matter interactions. *Phys. Rev. X* **11**, 021050 (2021).

**Publisher's note** Springer Nature remains neutral with regard to jurisdictional claims in published maps and institutional affiliations.

**Open Access** This article is licensed under a Creative Commons Attribution 4.0 International License, which permits use, sharing, adaptation, distribution and reproduction in any medium or format, as long as you give appropriate credit to the original author(s) and the source, provide a link to the Creative Commons licence, and indicate if changes were made. The images or other third party material in this article are included in the article's Creative Commons licence, unless indicated otherwise in a credit line to the material. If material is not included in the article's Creative Commons licence and your intended use is not permitted by statutory regulation or exceeds the permitted use, you will need to obtain permission directly from the copyright holder. To view a copy of this licence, visit <http://creativecommons.org/licenses/by/4.0/>.

© The Author(s) 2024



## Methods

### Sample fabrication

The suspended SiC films were purchased from Silson. The spiral ridges were fabricated with standard electron-beam lithography followed by electron-beam deposition. First, the substrates were cleaned with O<sub>2</sub> plasma and spin coated with 120 nm of 950K polymethyl methacrylate. Subsequently, the masks were fabricated under electron-beam exposure. After the post-exposure development of the masks, the substrate was descummed with O<sub>2</sub> plasma before the electron-beam deposition of 30 nm Cr. The structures were finally realized by lifting off the polymethyl methacrylate masks in acetone for several hours.

### Transmission sSNOM

Near-field maps are obtained with a commercial sSNOM setup (Neaspec) equipped with a pseudo-heterodyne interferometer to obtain amplitude- and phase-resolved images. The light source used in the experiments is an optical parametric oscillator laser (Stuttgart Instruments) powered by a pump laser at  $\lambda = 1,035$  nm with 40 MHz repetition rate and ~500 fs pulses. The mid-IR output is obtained by difference-frequency generation in a nonlinear crystal between the signal and idler outputs of the optical parametric oscillator and its frequency bandwidth (around 100 cm<sup>-1</sup> at 11  $\mu$ m) is reduced using a monochromator (below 3 cm<sup>-1</sup>, limited by the interferometer we use for the measurement). A quarter-wave plate (Optogama) specifically designed to cover the SiC Reststrahlen band (~800–950 cm<sup>-1</sup> or ~12.5–10.5  $\mu$ m) is used to convert the linear polarized output of the mid-IR laser source (Stuttgart Instruments) to RCP and LCP light. The beam is loosely focused at normal incidence by a parabolic mirror positioned below the sample. The near-field signal is scattered by a metal-coated (Pt/Ir) AFM tip (Arrow-NCPt, NanoWorld) oscillating at a frequency of  $\Omega \approx 280$  kHz, and collected by a second off-axis parabolic mirror positioned above the sample. The tapping amplitude was set to ~80 nm and the signal demodulated at the second harmonic ( $2\Omega$ ) for background suppression. Before focusing, half of the light is redirected towards a pseudo-heterodyne interferometer used to retrieve both amplitude and phase of the signal. The light scattered by the tip is recombined with the interferometer reference arm by a second beamsplitter and directed towards a nitrogen-cooled mercury cadmium telluride infrared detector.

### Simulations

The simulated vortex maps are obtained with a custom-written MATLAB (v. R2023a) code by using the Huygens principle (Supplementary Note 3). For each simulation, at least  $N = 300$  individual sources are used. The dielectric function of SiC is modelled as follows:

$$\varepsilon(\omega) = \varepsilon_{\infty} \left( 1 + \frac{\omega_{\text{LO}}^2 - \omega_{\text{TO}}^2}{\omega_{\text{TO}}^2 - \omega^2 - i\gamma\omega} \right), \quad (3)$$

where  $\omega_{\text{TO}} = 797$  cm<sup>-1</sup>,  $\omega_{\text{LO}} = 973$  cm<sup>-1</sup>,  $\varepsilon_{\infty} = 6.6$  and  $\gamma = 6.6$  cm<sup>-1</sup>. The value of  $\gamma$  is somewhat higher than what has been recently estimated for SiC membranes<sup>38</sup>, but we use it as it better reproduces the experimental data. The SPHP wavevector in the SiC membranes is numerically

calculated from the implicit equation for the anti-symmetric mode in polaritonic isotropic thin films<sup>38</sup>.

### Data availability

The data supporting the findings of this study are available in the Article and its Supplementary Information and via Zenodo at <https://doi.org/10.5281/zenodo.10557842>. Additional data are available from the corresponding authors upon reasonable request.

### Code availability

Code for the simulations is available via Zenodo at <https://doi.org/10.5281/zenodo.10557842>. Additional codes are available from the corresponding authors upon reasonable request.

### Acknowledgements

S.A.M. acknowledges the Deutsche Forschungsgemeinschaft (MA 4699/7-1 and MA 4699/9-1), the Australian Research Council (DP220102152) and the Lee Lucas Chair in Physics. R.B. acknowledges the National Council for Scientific and Technological Development (CNPq, PDJ 2019–150393/2020-2). H.R. acknowledges funding support from the Australian Research Council (DECRA Project DE220101085). This work was performed in part at the Melbourne Centre for Nanofabrication (MCN) in the Victorian Node of the Australian National Fabrication Facility (ANFF). L.N. and E.C. acknowledge funding from the European Commission through the ERC Starting Grant CATALIGHT (802989), the Deutsche Forschungsgemeinschaft (EXC 2089/1–390776260) via e-conversion cluster of excellence, the Bavarian program Solar Energies Go Hybrid (SolTech) and the Center for NanoScience (CeNS).

### Author contributions

A.M., H.R. and R.B. conceived the idea. L.N. fabricated the samples. A.M. performed the measurements. A.M. and H.R. analysed the data and carried out the theoretical simulations. S.A.M. and E.C. supervised the project and acquired the funding. A.M. and H.R. wrote the manuscript with input from all authors. All authors contributed to the discussion.

### Competing interests

The authors declare no competing interests.

### Additional information

**Supplementary information** The online version contains supplementary material available at <https://doi.org/10.1038/s41566-024-01410-5>.

**Correspondence and requests for materials** should be addressed to Andrea Mancini, Haoran Ren or Stefan A. Maier.

**Peer review information** *Nature Photonics* thanks Yuanjie Yang and the other, anonymous, reviewer(s) for their contribution to the peer review of this work.

**Reprints and permissions information** is available at [www.nature.com/reprints](http://www.nature.com/reprints).